On the propagation of viscous gravity currents of non-Newtonian fluids in channels with varying cross section and inclination

S. Longo[a], L. Chiapponi[a], V. Di Federico[b]

[a1]*Dipartimento di Ingegneria Civile, Ambiente Territorio e Architettura (DICATeA), Università di Parma, Parco Area delle Scienze, 181/A, 43124 Parma, Italy*
[b2]*Dipartimento di Ingegneria Civile, Chimica, Ambientale e dei Materiali (DICAM), Università di Bologna, Viale Risorgimento, 2, 40136 Bologna, Italy*

Abstract

This paper presents a model for the laminar propagation of gravity currents of rheologically complex fluids over natural slopes. The study is motivated by the ubiquitous occurrence of gravity currents in environmental applications that are confined by channels that widen and have reduced slopes in the flow direction; typical examples are mud and lava flows. In these applications, many fluids exhibit nonlinear relationships between shear stress and shear rate, with or without the appearance of a yield stress. We consider Ostwald-de Waele and Herschel-Bulkley fluids. A power-law equation is used to capture the variations in the channel shape and slope in the flow direction. We study the motion of constant and time-dependent volumes of these fluids on smoothly varying topographies. Approximate similarity solutions are obtained for Ostwald-de Waele fluids, while for HB fluids, we use the methods of characteristics to compute front propagation. Constant volume and constant influx tests were conducted in a channel with a widening parabolic cross-section and an inclination decreasing downstream from $\approx 7°$ to $\approx 3.2°$. The front position was measured continuously over time, and the current thickness and the surface velocity were recorded for a subset of experiments in some cross sections. The experimental study confirms the theoretical formulation, with a better agreement for constant influx than constant volume currents.

Keywords: gravity current, method of characteristics, non-Newtonian, laboratory experiments

1. Introduction

The propagation of gravity currents in the environment has been widely studied due to its relevant theoretical and practical implications. The development of adequate models makes it possible to describe complex natural phenomena and to devise appropriate prevention and mitigation measures. Several examples of gravity currents in meteorology, oceanography, earth sciences and industrial processes are listed by Simpson [1]: thunderstorm outflows, sea-breeze fronts, gases in mines, ventilation flows, salt wedges in estuaries, turbidity plumes in lakes and reservoirs, power station effluents, oil slicks, avalanches, debris and mudflows, and lava streams. Many environmental fluids involved in these applications exhibit nonlinear relationships between shear stress and shear rate, without or with the appearance of a yield stress. In the former case, the preferred rheological model is the Ostwald-de Waele power-law relationship; in the latter, the Herschel-Bulkley (HB) model is preferred. For suspensions of fine cohesive sediments (silt or clay) a non-negligible yield stress typically appears beyond a certain concentration [2]. The typical cases of environmental non-Newtonian currents are mud-flow waves propagating down natural slopes [3], mud slurries resulting from dredging [4] or mining [5] transported to disposal and tailings areas, fluids employed in fracing technology flowing in subterranean fractures [6], debris flows triggered by rainfall events [7], and lava flows [8].

A paramount distinction in the study of gravity currents is between viscous and inviscid. In the former case, viscous forces prevail over inertia and the balance is between gravitational and viscous effects; in the latter case, inertia is dominant over viscous forces, and the current behaviour is determined by the interplay of gravity and inertia. The same current can undergo a transition from inviscid to viscous or, more rarely, from viscous to inviscid [9]; the inertial to viscous transition for a power-law non-Newtonian fluid was observed experimentally by Chowdhury and Testik [10].

The objective of the present paper is to analyse viscous gravity currents of non-Newtonian fluids in a natural environment, motivated by the observation of natural phenomena such as debris, mud, and lava flows down a slope. The reference model, valid for a Newtonian fluid, is the viscous two-dimensional gravity current of time-variable volume propagating over an horizontal rigid plane [11] or down a slope [12]. Takagi and Huppert [13] considered viscous Newtonian flow in channels of finite width and constant cross-section, incorporating the effect of the channel shape and showing its influence on the front

2

velocity of the current. They extended the model upon allowing the channel cross section to vary longitudinally in a continuous fashion [14]. Longo et al. [15] and [16] solved a similar problem for a power-law non-Newtonian fluid.

When the rheological model involves a nonzero yield stress, the flow characteristics are harder to predict as solid and liquid regions of a permanent or transient nature appear [17]. The behaviour of two-dimensional gravity currents of viscoplastic fluids was modelled analytically by Hogg and Matson [18] and numerically by Huang and Garcia [3], Vola et al. [19], and Balmforth et al. [20]. The coupled influence of a finite channel width on viscoplastic flow down a slope was explored by Mei and Yuhi [21] and Cantelli [22], who adopted a Bingham rheological model. Flows of viscoplastic fluids down uniform slopes were investigated experimentally by Ancey and Cochard [23] and Chambon et al. [24], among others.

Based on these efforts, we aim at advancing the state of the art on non-Newtonian flows over natural slopes by improving the description of the basal topography and of fluid rheology [25]. We model a channel that widens and reduces its slope along the flow direction. This is the case of mud-flows and debris flows spreading through hillslope incisions, as gullies and ravines progressively enlarge and reduce their slope until the alluvial fan is reached [26]. On volcanic cones, molten lava erodes the ground it flows over and self-organises into channels [27], that have decreased slopes in the flow direction [28]. Hence, we consider one-dimensional gravity currents of non-Newtonian fluids, which are described by the power-law (Ostwald-de Waele) model, flowing in channels with various shapes, which are described by the parameter k. The channel cross section and slope are allowed to vary along the flow direction according to two additional parameters b and ω. The volume of the current varies over time according to the parameter α. Note that the combination of a widening cross section and a decreasing slope along the flow direction is a non-trivial extension of earlier models [14, 16] and constitutes a novel development for Newtonian flow. Solutions derived in semi-analytical format are self-similar and allow for a quick assessment of the spatiotemporal development of the gravity current, which can be used as a benchmark for more complex numerical models (if the transverse dynamics can be neglected).

The impact of more realistic rheological models is investigated upon substituting the power-law constitutive equation with the HB model and considering the presence of slip effects [29]. The resulting problem is then solved numerically by employing an algorithm based on the method of characteris-

3

tics.

Theoretical results are validated by laboratory experiments, conducted both with power-law and HB fluids; in the latter case, different methods for measuring the yield stress are employed and compared.

The structure of the paper is as follows. Section 2 formulates the problem in dimensionless form for a non-Newtonian power-law fluid; Newtonian flow is a special subcase. The solution, obtained via the method of characteristics, is presented and discussed in Section 3. The formulation is extended to the flow of an HB fluid with yield stress in Section 4. The laboratory setup and experimental results are presented in Section 5. A set of conclusions, including recommendation for future work, is drawn in Section 6. Appendix A contains details on the rheometric measurements, Appendix B includes an analysis of the dependence of the rate of advancement on model parameters for power-law currents, and Appendix C describes an extension of the model for HB fluids to take slip effects into account.

2. Theory

2.1. Currents in power-law fluids

Consider a gravity current of a non-Newtonian Ostwald-deWaele fluid injected in a straight channel, whose longitudinal slope and cross section vary along the flow direction (see Figure 1). A locally orthogonal coordinate system (x,y,z) is adopted for the analysis, with x along the channel axis, z normal to the slope, and y across the channel.

As the longitudinal slope of the channel varies with x, the line joining the lowest points along the channel length (thalweg in fluvial engineering) is curvilinear; its inclination angle $\beta(x)$ with respect to the horizontal is given by

$$\sin \beta = \sin \beta_0 \left(\frac{x}{mx^*} \right)^\omega, \tag{1}$$

where x^* is a length scale, β_0 is the inclination angle at $x = mx^*$, m is a coefficient introduced for convenience, and ω is a positive/negative constant representing an increasing/decreasing bed slope along the flow direction, the latter case being the most common in environmental applications.

The channel cross section, taken to be symmetric, varies continuously along x; in the local coordinate system, the cross section walls are described by the function $d(x,y) = (rx^b)^{1-k}|y|^k$, where k is a parameter describing the

4

shape, b is a non-negative exponent governing its longitudinal variation, and r (dimensions $[L^{1-b}]$) is a constant coefficient; rx^b is thus the channel length scale, whose variation in the x direction is controlled by both r and b. As to the shape, the wall profile is convex, rectilinear or concave depending on whether $k < 1$, $k = 1$ or $k > 1$. Thus, $k = 1$ describes a triangular cross section, while $k < 1$ and $k > 1$ describe narrow and wide channels, respectively. In wide channels, the transverse dimension prevails over the vertical; the reverse is true in narrow channels. Relevant cases of wide channels are $k = 2$, which locally approximates a circular section with radius $rx^b/2$, and $k \to \infty$, corresponding to a rectangular cross-section with semi width rx^b. As to the longitudinal variation, the special case $b = 0$ corresponds to a constant cross-section, while for $b > 0$ wide channels ($k > 1$) tend to broaden and narrow channels ($k < 1$) to squeeze along the flow direction.

The fluid is released at the upper end of the channel; for convenience, the release is assumed to occur in the initial cross section, even though release over a finite channel length can in principle be accounted for (see, e.g., [23]). The volume of the current varies over time as $\propto t^\alpha$, where $\alpha = 0$ indicates a fixed volume, $\alpha = 1$ a constant influx, and $\alpha \gtrless 1$ an increasing or decreasing influx. Cases with $\alpha > 1$ are less common than $\alpha < 1$ for environmental currents; they can be observed in the initial stages of volcanic eruptions, as the eruption rate decreases with time [30].

It is assumed that the current is always contained by the channel walls; at a certain distance from the inlet section, the current height h is taken to be uniform in the transverse direction y and thin compared to its length, i.e., $h = h(x,t)$ with $h(x,t) \ll x_N(t)$, where $x_N(t)$ is the position of the front end of the current. In this regime, the top width of the advancing current is given by $2W(x,t) = 2h^{1/k}r^{1-1/k}x^{b(1-1/k)}$. The length scale in the transverse direction y is much smaller than the length scale in the direction of propagation x. In wide channels ($k > 1$), the current is thin with respect to the transverse length scale ($h \ll W$); the reverse is true in narrow channels ($k < 1$). Viscous forces prevail over inertia and the balance is between gravitational effects and viscous effects. The latter condition is verified at negligible distances from the inlet for constant influx ($\alpha = 1$), and at short distances for dam-break flows ($\alpha = 0$).

Under the previous assumptions, the pressure within the current is hydrostatic and equal to

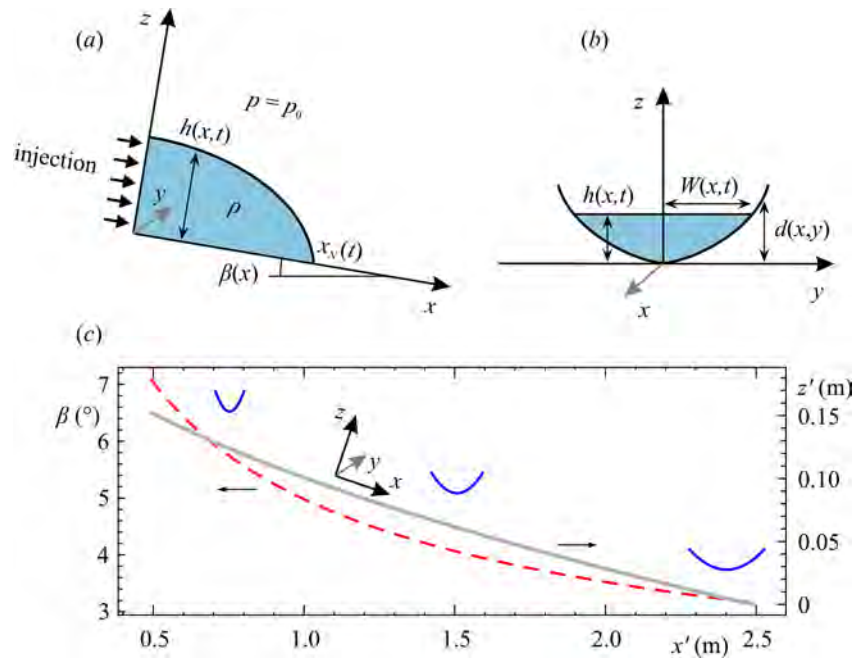$$p = p_0 + \rho g(h - z)\cos\beta, \tag{2}$$

5

Figure 1: (a) side view of the current and (b) cross-section of the channel; (c) line joining the lowest points along the channel length (tangent to the local coordinate x in the propagation direction, solid curve) and the channel slope (dashed curve, red online) for $\omega <= -1/2$ (decreasing slope). The cross-sections sketched at different abscissae (blue online) refer to a wide cross-section broadening downstream with $k = 2$ and $b > 0$. x' and z' are the lab coordinates.

where p_0 is the atmospheric pressure at the free surface, g is gravity, and ρ the fluid density. The motion is one-dimensional along the channel axis x with a section-average velocity $U(x,t)$. The momentum balance equation simplifies to

$$-\frac{\partial p}{\partial x} + \rho g \sin \beta + \frac{\partial \tau_{yx}}{\partial y} + \frac{\partial \tau_{zx}}{\partial z} = 0, \tag{3}$$

where τ_{yx} and τ_{zx} are the shear stresses. For a power-law fluid, these are given by $\tau_{yx} = \widetilde{\mu}\dot{\gamma}_{yx}|\dot{\gamma}_{yx}|^{n-1}$ and $\tau_{zx} = \widetilde{\mu}\dot{\gamma}_{zx}|\dot{\gamma}_{zx}|^{n-1}$, respectively, where $\dot{\gamma}_{yx}$ and $\dot{\gamma}_{zx}$ are the shear rates, $\widetilde{\mu}$ the consistency coefficient, and n the fluid behaviour index ($n = 1$ for a Newtonian fluid, $n < 1$ and $n > 1$ for shear-thinning/thickening fluids, respectively).

In the following, only the case of wide channels ($k > 1$) will be considered, given the focus on surface channels over natural slopes. Hence, the assumption $h \ll W$ implies $\partial \tau_{yx}/\partial y \ll \partial \tau_{zx}/\partial z$, and the third term on the l.h.s. of (3) can be neglected.

Substituting the shear stress expressions and the pressure distribution (2) in the simplified version of eq. (3) valid for a wide channel yields

$$\frac{\partial}{\partial z}\left[\left(\frac{\partial u}{\partial z}\right)^n\right] = -S, \tag{4}$$

where S is the source term, equal to

$$S = -\frac{\rho g}{\widetilde{\mu}}\frac{\partial h}{\partial x} + \frac{\rho g}{\widetilde{\mu}}\sin \beta_0 \left(\frac{x}{mx^*}\right)^\omega. \tag{5}$$

By imposing the boundary conditions

$$u = 0 \ (z = d), \partial u/\partial z = 0 \ (z = h), \tag{6}$$

the integration of eq. (4) yields

$$u(x,y,z,t) = S^{1/n}\frac{n}{n+1}\left[(h(x,t) - d(x,y))^{(n+1)/n} - (h(x,t) - z)^{(n+1)/n}\right]. \tag{7}$$

The cross-sectional area occupied by the current is

$$A(x,t) = 2\int_0^{W(x,t)}[h(x,t) - d(x,y)]\,\mathrm{d}y = \frac{2k}{k+1}r^{(1-1/k)}x^{b(1-1/k)}h^{(1+1/k)}, \tag{8}$$

7

and the volume flux is

$$Q(x,t) = 2 \int_0^{W(x,t)} \mathrm{d}y \int_{d(x,y)}^{h(x,t)} u(x,y,z,t)\mathrm{d}z$$

$$= 2\mathrm{B}\left[2 + \frac{1}{n}, 1 + \frac{1}{k}\right] r^{(1-1/k)} S^{1/n} x^{b(1-1/k)} h^{2+1/k+1/n}, \quad (9)$$

where $\mathrm{B}[.,.]$ is the Beta function.

The local continuity equation for a one dimensional current is

$$\frac{\partial A}{\partial t} + \frac{\partial Q}{\partial x} = 0, \tag{10}$$

also equivalent to

$$2W \frac{\partial h}{\partial t} + \frac{\partial Q}{\partial x} = 0, \tag{11}$$

because $\partial A/\partial t = 2W \partial h/\partial t$.

The problem formulation is completed by the mass balance equation

$$\int_0^{x_N(t)} A \, \mathrm{d}x = q t^\alpha, \tag{12}$$

where $q t^\alpha$, $(q > 0, \alpha \geq 0)$ is the volume of fluid released. At $x = x_N(t)$, the current height vanishes, i.e.

$$h\left[x_N(t), t\right] = 0. \tag{13}$$

It is then assumed that between the two terms driving the motion included on the r.h.s. of eq. (5), gravity prevails over the slope of the free surface. This assumption is true in most of the flow domain except near the front of the current, where discrepancies with the present model are due to the effects of curvature of the free surface. Neglecting the first term on the r.h.s. of eq. (5), and substituting the simplified eq. (5) and eq. (9) into eq. (11) yields

$$h^{1/k} x^{b(1-1/k)} \frac{\partial h}{\partial t}$$

$$+ \mathrm{B}\left[2 + \frac{1}{n}, 1 + \frac{1}{k}\right] \left(\frac{\rho g}{\widetilde{\mu}}\right)^{1/n} \frac{(\sin \beta_0)^{1/n}}{(m x^*)^{\omega/n}} \frac{\partial}{\partial x} \left[x^{\omega/n + b(1-1/k)} h^{(2+1/k+1/n)}\right] = 0. \tag{14}$$

The boundary condition at the front of the current, eq. (13), is not satisfied. Physically, the resulting model does not represent the behaviour of the profile close to the front end, as in reality surface tension (not included in the model) smooths the profile down to the zero value and the slope of the free surface cannot be further neglected.

Substituting eq. (8) into eq. (12) yields

$$\frac{2k}{k+1} r^{(1-1/k)} \int_0^{x_N(t)} x^{b(1-1/k)} h^{(1+1/k)} \mathrm{d}x = q t^\alpha. \tag{15}$$

The problem is solved in dimensionless form. Introducing the length scale

$$x^* = \left[\frac{(k+1)q}{2k\mathrm{B}^\alpha r^{(1-1/k)}} \right]^{kn/l} \left(\frac{\widetilde{\mu} m^\omega}{\rho g \sin \beta_0} \right)^{k\alpha/l}, \quad l = [b(k-1)+2k+1]n+\alpha k, \tag{16}$$

and the time scale

$$t^* = \frac{1}{\mathrm{B}} \left[\frac{(k+1)q}{2k\mathrm{B}^\alpha r^{(1-1/k)}} \right]^{-k/l} \left(\frac{\widetilde{\mu} m^\omega}{\rho g \sin \beta_0} \right)^{[b(k-1)+2k+1]/l}, \tag{17}$$

where B indicates the Beta function with the argument appearing in eq. (9), eqs. (14-15) become, respectively,

$$H^{1/k} X^{b(1-1/k)} \frac{\partial H}{\partial T} + \frac{\partial}{\partial X} \left[X^{[\omega/n+b(1-1/k)]} H^{(2+1/k+1/n)} \right] = 0, \tag{18}$$

$$\int_0^{X_N(T)} X^{b(1-1/k)} H^{1+1/k} \, \mathrm{d}X = T^\alpha, \tag{19}$$

where dimensionless variables are defined as $H = h/x^*$, $X = x/x^*$, $X_N = x_N/x^*$, $T = t/t^*$.

A solution to the system of PDEs formed by eqs. (18-19) is sought with the method of characteristics. Eq. (18) can be written in standard form as

$$a(H, X) \frac{\partial H}{\partial X} + b(H, X) \frac{\partial H}{\partial T} = f(H, X), \tag{20}$$

and along the characteristic curve $dX/dT = a/b$ eq. (20) reduces to the ordinary differential equation $dH/dX = f/a$ or to $dH/dT = f/b$ [see, e.g., 31].

In general, a numerical integration is required; however, eq.(18) admits the analytical solution

$$H(X,T) = c_1 X^{(n-\omega)/(n+1)} T^{-n/(n+1)}, \tag{21}$$

with

$$c_1 = \left[\frac{n}{(n+1)\delta}\right]^{n/(n+1)}, \quad \delta = \frac{n(k+1) + k(n+1) + b(k-1)(n+1) - \omega(k+1)}{k(n+1)}. \tag{22}$$

The integration of the mass balance equation (19) yields the dimensionless position of the current front as

$$X_N = \left[\frac{\delta}{c_1^{(1+1/k)}}\right]^{1/\delta} T^{[\alpha k(n+1)+n(k+1)]/[k(n+1)\delta]} = F_1 T^{F_2}, \tag{23}$$

in which $F_2 = F_2(\alpha, n, k, \omega, b)$ is the propagation rate of the current with time; its dependency on the model parameters is discussed in Appendix B. For $\omega = 0$, eqs. (21) and (23) are coincident with the expressions given for constant slope by Longo et al. [16]; for $\omega = 0$ and $n = 1$, they further reduce to the solution given in dimensional form by Takagi and Huppert [13].

It is observed that the thickness of the current resulting from eq. (21) has its maximum value at $X = X_N$. As earlier noted, this is not true due to the effects of the curvature of the free surface and surface tension; however, there is experimental evidence that a current flowing in inclined channels experiences a fast growth near the front [see 16].

2.2. Currents of a Herschel-Bulkley fluid

The presence of a non-negligible yield stress τ_0 modifies the power-law into the HB rheological model, with a stress-strain relation given by

$$\tau_{ij} = \left(\tilde{\mu}|\dot{\gamma}|^{n-1} + \frac{\tau_0}{|\dot{\gamma}|}\right)\dot{\gamma}_{ij} \quad \text{for} \quad |\tau| > \tau_0, \tag{24}$$

where $|\dot{\gamma}| = \sqrt{II_{\dot{\gamma}}/2}$ and $|\tau| = \sqrt{II_\tau/2}$, with $|(...)|$ representing the magnitude of the tensor expressed by introducing its second invariant $II_{(...)}$. The material flows only when the magnitude of the extra stress tensor exceeds the yield stress value. Figure 2 shows the geometry of the current in steady uniform flow, with a yield surface of height h_s separating the sheared region
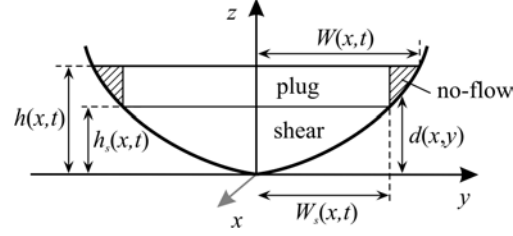
Figure 2: Cross-section of the channel with a current of fluid in presence of a yield stress.

(of width $2W_s$) from the plug, and a near wall, motionless region between the free surface and the yield surface. In unsteady conditions, rigorously the velocity in the transverse direction y cannot be neglected and the free surface and the yield surface vary along y [21]. However, in the present model we assume that the dynamics in the transverse (y) direction is negligible and that $\partial h/\partial y = \partial h_s/\partial y = 0$.

Assuming again that the cross section is 'wide' ($k > 1, b \geq 0$), the adoption of the rheological model (24) for the sheared flow region in eq. (3) yields

$$\frac{\partial}{\partial z}\left[\left(\frac{\partial u}{\partial z}\right)^n\right] = -S, \quad \text{for} \quad d(x,y) \leq z \leq h_s(x,t) \tag{25}$$

with the boundary conditions

$$u = 0, \quad z = d(x,y) \tag{26}$$

and

$$\frac{\partial u}{\partial z} = 0, \quad z = h_s(x,t). \tag{27}$$

Integrating eq. (25) with (26)-(27) yields

$$u(x,y,z,t) = S^{1/n}\frac{n}{n+1}\left[(h_s(x,t)-d(x,y))^{(n+1)/n} - (h_s(x,t)-z)^{(n+1)/n}\right], \tag{28}$$

which is identical to eq. (7) upon substituting h with h_s. The volume flux in the sheared region, Q_s, is again identical to eq. (9) upon substituting h with h_s:

$$Q_s(x,t) = 2\int_0^{W(x,t)} \mathrm{d}y \int_{d(x,y)}^{h_s(x,t)} u(x,y,z,t)\mathrm{d}z$$

$$= 2\mathrm{B}\left[2+\frac{1}{n}, 1+\frac{1}{k}\right] r^{(1-1/k)}S^{1/n}x^{b(1-1/k)}h_s^{2+1/k+1/n}. \tag{29}$$

11

In the plug region, the velocity $u_p(x, y, t)$ is independent of z and equal to $u_p = u(x, y, h_s, t)$:

$$u_p(x, y, t) = S^{1/n} \frac{n}{n+1} (h_s(x, t) - d(x, y))^{(n+1)/n}. \tag{30}$$

The volume flux in the plug, Q_p, is obtained by integration as

$$Q_p(x, t) = 2 \int_0^{W_s(x,t)} \mathrm{d}y \int_{h_s(x,t)}^{h(x,t)} u_p(x, y, t) \mathrm{d}z$$

$$= 2\mathrm{B} \left[2 + \frac{1}{n}, 1 + \frac{1}{k} \right] \frac{2kn + k + n}{k(n+1)} r^{(1-1/k)} S^{1/n} x^{b(1-1/k)} (h - h_s) h_s^{(1+1/n+1/k)}. \tag{31}$$

Hence, the total volume flux is

$$Q \equiv Q_p + Q_s$$

$$= 2\mathrm{B} \left[2 + \frac{1}{n}, 1 + \frac{1}{k} \right] r^{(1-1/k)} S^{1/n} x^{b(1-1/k)} h_s^{1+1/k+1/n} \left[h + \frac{n(k+1)}{k(n+1)} (h - h_s) \right]. \tag{32}$$

For $n = 1$ and $\tau_0 \neq 0$ (Bingham fluid), $b = 0$ (uniform section in the x direction), $\omega = 0$ (constant bed slope), and $k \to \infty$ (rectangular cross-section of width $2r$), the expression (2.13) in Liu and Mei [32] is recovered after the pressure gradient in the streamwise direction is neglected. Under steady-state flow, eq. (32) was earlier derived by Cintoli et al. [33].

Special attention should be devoted to the boundary condition at the bottom. Numerous experiments have shown that slip occurs near the walls due to migration of polymers or particles from high shear regions [29]. The phenomenon occurs also in real environmental flows (lavas and glaciers) where the motion occurs with a sequence of solidification and melting which produce a slip [34]. As a working assumption, we neglect the slip contribution when comparing theory and experiments. Appendix C describes the extension of the model to take slip effects into account.

On the yield surface, $\tau_{xz} = \pm \tau_0$, which results in

$$h_s(x, t) = h(x, t) + \frac{\tau_0 \operatorname{sgn} u}{\rho g \cos \beta(x)(\partial h / \partial x) - \rho g \sin \beta(x)}. \tag{33}$$

Assuming again that the channel slope is dominant with respect to the free-surface gradient, eq. (33) simplifies into

$$h_s(x,t) = h(x,t) - \frac{\tau_0}{\rho g \sin \beta(x)}. \tag{34}$$

where the velocity u is taken to be positive. Introducing the expression of the channel inclination (1) into (34) yields

$$h_s(x,t) = h(x,t) - \frac{\tau_0}{\rho g \sin \beta_0} \left(\frac{x}{mx^*}\right)^{-\omega} \equiv h - h_c \left(\frac{x}{mx^*}\right)^{-\omega}, \tag{35}$$

where $h_c = \tau_0/(\rho g \sin \beta_0)$ is the threshold depth of a layer about to flow down an inclined plane of slope β_0. Considering that the channel slope varies along the flow direction, this entails an increment (reduction) of the thickness of the plug downstream if $\omega < 0 (> 0)$ (inclination decreasing/increasing with x).

Substituting eq. (32) into eq. (11), and neglecting the inclination of the free surface in the source term of eq. (5) results in

$$h^{1/k} x^{b(1-1/k)} \frac{\partial h}{\partial t} + \frac{\partial}{\partial x} \left[\text{B} \left[2 + \frac{1}{n}, 1 + \frac{1}{k} \right] \left(\frac{\rho g}{\tilde{\mu}}\right)^{1/n} \frac{(\sin \beta_0)^{1/n}}{(mx^*)^{\omega/n}} \right.$$
$$\left. \times x^{\omega/n+b(1-1/k)} h_s^{(1+1/k+1/n)} \left(h + \frac{n(k+1)}{k(n+1)} (h - h_s) \right) \right] = 0, \tag{36}$$

while the boundary condition (13) and the mass balance equation (15) are unvaried. Utilising the same length and time scales defined in (16) and (17), and defining $H_s = h_s/x^*$ and $H_c = h_c/x^*$, yields in dimensionless form

$$H_s = H - H_c \left(\frac{X}{m}\right)^{-\omega} \tag{37}$$

$$H^{1/k} X^{b(1-1/k)} \frac{\partial H}{\partial T}$$
$$+ \frac{\partial}{\partial X} \left[X^{\omega/n+b(1-1/k)} H_s^{1+1/k+1/n} \left(H + \frac{n(k+1)}{k(n+1)} (H - H_s) \right) \right] = 0. \tag{38}$$

The global mass balance equation (19) is unchanged.

13

A solution to eq. (38) with the constraint represented by eq. (19) is sought numerically employing an algorithm based on the method of characteristics. The chosen dependent variable is H_s, and the partial differential equation is transformed into an ordinary one in the time domain along the single characteristic curve propagating downstream. The spatial domain is discretised into a uniform grid (500 points in most computations) extending from the source to the front end of the advancing current; computations are performed at each time step. The initial condition is computed by neglecting the yield stress and the slip effect, adopting the analytical solution represented by eq. (21) with a front end position given by eq. (23). A boundary condition at the injection section is obtained by equating the depth of the current to the normal depth of the instantaneous flux.

As a final comment, we recall that the existence of a plug layer implies some inconsistencies in the description of the flow. These inconsistencies are overcome by admitting a pseudo-plug as described by Walton & Bittleston [35], and a pseudo-plug and fake yield surfaces, as further discussed in [36]. In the pseudo-plug model, higher order terms are associated with a weak yield instead of a rigid motion.

3. The experiments

To test the theoretical formulation, a channel with a decreasing bottom inclination and a longitudinally variable, parabolic cross-section was machined out of medium-density poliurethane using a CNC milling cutter. The channel is 200 cm long with cross-section characterised by $k = 2$ (a parabola, locally approximated by a circle) and linearly enlarging downstream ($b = 1$) with parameter $r = 0.2$. The channel has an inclination $\beta_0 = 5°$ at a distance $x_0 = 100$ cm from the virtual origin, which is located 50 cm upstream of the initial section. The parameter controlling the variation of the bottom inclination, $\sin \beta(x) = \sin \beta_0 (x/x_0)^\omega$, is $\omega = -1/2$. Hence, the channel inclinations are $\beta \approx 7°$ in the initial section ($x = 50$ cm) and $\beta \approx 3.2°$ in the end section ($x = 250$ cm). The line joining the lowest points along the channel length and the angle of inclination of the experimental channel versus the lab coordinate are shown in Figure 1. Figure 3 depicts the experimental layout, with a photo showing the advancement of the current.

The laboratory tests were performed with constant volume ($\alpha = 0$) and constant inflow ($\alpha = 1$). In the first case, a nearly instantaneous release (dam-break) was obtained with a lock gate located 16 cm from the inlet
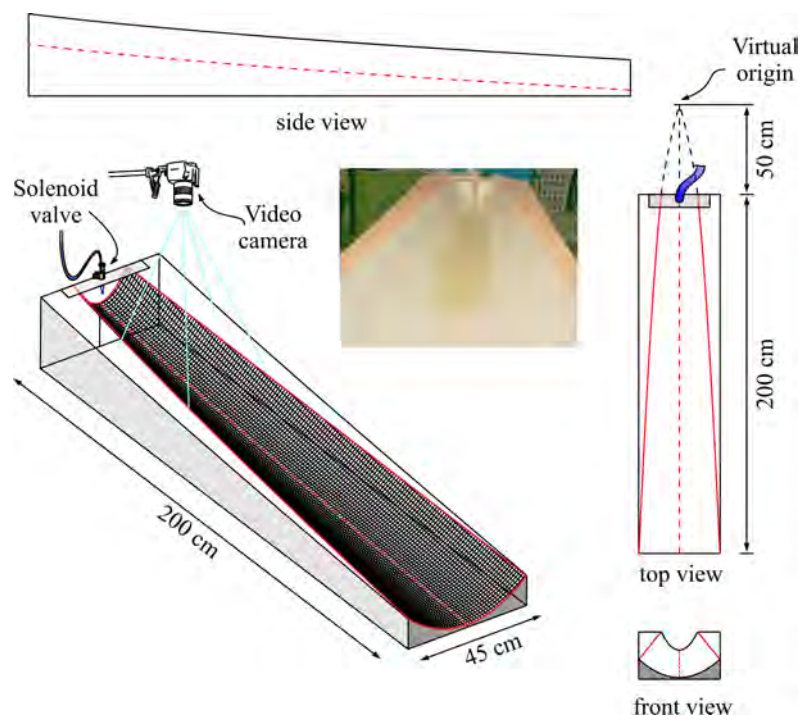
Figure 3: The experimental layout; the insert shows a photograph of the advancing current.

section; the volume of released fluid was measured by weighing the mass initially stored in the lock with an accuracy of 1.5%. The constant flow rate required by tests with $\alpha = 1$ was obtained employing a diaphragm pump or a rotating vane pump (for the fluids with larger viscosity), with the hydraulic circuit controlled by solenoidal valves; this allowed an electronic control of the timing. The flow rate was estimated by measuring the weight variation of the container filled with the test fluid, directly on the plate of an electronic scale, with an overall accuracy better than 1%. Some tests with shear thickening fluid were performed by directly pouring the liquid through funnels of different size with an accuracy in the average discharge of 1.5%.

The position of the current front was detected by employing an HD video camera (1980×1020 pixels) with a frame rate of 25 Hz, observing the front with respect to a rule drawn directly on the channel bottom and having a space step of 5 cm between the marks. A smaller space step was judged unnecessary due to the relatively low speed of the front of the current in most tests. The most advanced tip of the current (positioned along the channel axis) was taken to indicate the front, even though the transverse average position of the front should be computed to be consistent with the assumptions. However, the associated error is negligible as the current advances; for most experiments, it is less than $\approx 3\,\mathrm{cm}$ near the inlet section and less than $\approx 1\,\mathrm{cm}$ near the end section of the channel.

For some tests, the thickness of the current was measured in two sections using an Ultrasound distance metre (Turck Banner Q45UR) with an accuracy of 0.03 cm and a time response of 10 ms [see 37, 38, for details on its accuracy]. Particle Image Velocimetry was also performed near the front of the current to measure the surface velocity. The image were taken from the video at 25 frames/s and then elaborated with an overall uncertainty in the velocity equal to 0.05 cm/s.

The Newtonian fluid used in the experiments was pure glycerol. Xanthan gum was added up to 0.1% (wt) to obtain shear-thinning fluids. The shear-thickening fluid was a mixture of water (45% wt) and cornstarch (55% wt). Water and Xanthan gum (0.8% and 1% wt), or water and Carbopol 980 (0.9% and 1.8% wt, non-neutralised) were used to obtain an HB shear-thinning fluid. Neutralisation of Carbopol mixtures allows obtaining thicker fluids with higher yield stress and consistency index, that is generally less sensitive to chemical disturbances and to ions. However, the non-neutralised mixtures were used within a short period after their preparation and rheometric measurements, taking care of the cleanliness of the tools and of the sur-
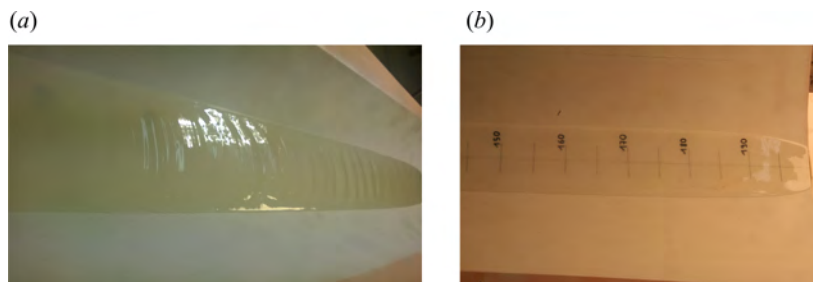
(a)   (b)

Figure 4: (a) Chevrons appearing on the free surface of a HB fluid in Experiment 26; (b) a HB fluid at rest in the channel 10 minutes after stopping the injection in Experiment 29.

faces. Details on the rheometric measurements, including methods adopted to measure the yield stress, are reported in Appendix A.

While the experiments with power-law fluids did not show any significant unexpected feature, some experiments with HB fluids showed some remarkable aspects in the free surface geometry. Figure 4a shows the HB fluid current during Experiment 26, with some characteristic chevrons that have been observed and analysed by Slim et al. [39] for a viscous fluid flowing in a channel and covered by an elastic plate or by a thin skin of very viscous fluid. A plausible explanation is an instability of the free surface layer due to the varying traction of the fluid flowing underneath, with a consequent out-of-plane buckling due to the associated in-plane shear. The inlet condition could also have contributed to the phenomenon. Figure 4b shows the residual fluid in the channel 10 minutes after stopping the injection for Experiment 29. The thickness of the residual layer of fluid is proportional to the yield stress and increases streamwise for constant yield stress.

4. Results and discussion

Two sets of experiments were conducted to validate the theoretical results. In the first set, power-law fluids were used, both dam-break ($\alpha = 0$) and constant inflow ($\alpha = 1$) conditions were considered, and the current front was measured over time. In the second set of experiments, HB fluids were used under the condition $\alpha = 1$, and the current front and profile (for some experiments) were recorded over time.

In comparing theory and experimental data on the position of the front, a time shift was introduced to account for factors affecting the initial stage

17

of propagation of dam-break flows ($\alpha = 0$), such as (i) the initial collapse of the fluid volume and (ii) the length of time to open the gate. It was also necessary to introduce a correction to account for the effective experimental conditions, that differ from theory: the volume of fluid was not a Dirac pulse but was stored in a finite length of the channel (from an abscissa of 50 cm - the distance of the starting section of the channel from the virtual origin - to 66 cm - the section of the lock). The shift was taken to be equal to the sum of two terms: i) the theoretical time requested for a Dirac volume in the origin to reach the section of the lock (always positive) and ii) a correction to include inertia effects (always negative, as inertia reduces the speed of the front). In order to avoid a subjective evaluation of the time shift, a fitting procedure was applied to minimise the residual between the theory and the experiments. The computed time shift was of a few seconds for the most viscous fluids. However, no adjustment of the rheometric parameters was requested, even though the time shift gave a degree of freedom in data fitting.

Parameters for the first set of experiments are listed in Table 1. The resulting position X_N of the front end of the current is shown in dimensionless form in Figure 5a (symbols) for $\alpha = 0$ and in Figure 5b (symbols) for $\alpha = 1$. The solid line represents perfect agreement with the theory. For $\alpha = 0$, good agreement between the theoretical model and the experiments becomes evident only in the late stage of propagation. In the early stage, lubrication theory is invalid because the depth-to-length ratio is not small. Then the current accelerates evolution towards the viscous regime. For this reason, the asymptotic theoretical line is reached from below in Figure 5a. For experiments with constant inflow rate ($\alpha = 1$), the position of the front shows a tighter agreement with the theory; discrepancies are attributed essentially to the variations of the rheometric parameters during time as a consequence of water evaporation.

Table 2 lists the parameters for the second set of experiments (HB fluids). Preliminarily, we note that the interpretation of the experiments with HB fluids requires special attention with respect to power-law fluids, because the yield stress is difficult to measure with accuracy. The best agreement between experiments and theory was obtained with a direct measurement of the yield stress (see, e.g., Experiments 29, 30 and 31). Direct measurement of the yield stress was performed for all the experiments. Moreover, water evaporation induced an increase over time of the yield stress and the consistency index. As a consequence, the front of the current was progressively decelerated. See

#	α	n	$\widetilde{\mu}$	ρ	q	
			$(\mathrm{Pa\,s}^n)$	$(\mathrm{kg\,m}^{-3})$	$(\mathrm{ml\,s}^{-\alpha})$	
1	0	1.00 ± 0.01	0.126 ± 0.005	1260	642	glyc
2	0	1.00	0.126	1260	267	glyc
4	0	1.47 ± 0.08	0.75 ± 0.07	1200	707	corn
14	0	0.53 ± 0.02	0.22 ± 0.01	1153	463	glyc-Xanth
15	0	0.53	0.22	1153	169	glyc-Xanth
16	0	0.53	0.22	1153	300	glyc-Xanth
3	1	1.47 ± 0.08	0.35 ± 0.03	1200	5.74	corn
5	1	1.47	0.88 ± 0.07	1200	19	corn
6	1	1.00 ± 0.01	0.126 ± 0.005	1260	0.92	glyc
7	1	1.00	0.40 ± 0.01	1260	6.93	glyc
8	1	1.00	0.40	1260	8.38	glyc
9	1	1.00	0.36 ± 0.01	1260	8.96	glyc
10	1	1.00	0.34	1260	4.13	glyc
11	1	0.57 ± 0.02	0.57 ± 0.02	1153	18.38	glyc-Xanth
12	1	0.57	0.57	1153	8.24	glyc-Xanth
13	1	0.57	0.57	1153	6.25	glyc-Xanth

Table 1: Parameter values for the experiments with power-law fluids. The last column indicates the fluid: pure glycerol (glyc), glycerol and Xanthan (glyc-Xanth), water (45% wt) and cornstarch (55% wt) (corn). The uncertainty listed for the rheometric parameters refers to one standard deviation.

Appendix A for a more detailed discussion.

Figure 6 shows a comparison between the experiments (symbols) and theory (solid lines) for HB fluids. The proposed model captures the propagation of the current front, with modest differences between theory and experiment; these discrepancies tend to decrease as time increases. The theoretical model represented in Figure 6 does not include slip effects, as their influence on the overall dynamics of the current in the present experiments (the surface of the channel has not been polished after milling, and has a roughness of the order of fractions of millimetres) are minimal and decidedly smaller than the uncertainties in the rheological parameters and in the overall geometry of the system.

A comparison between the theoretical and the experimental thickness is shown in Figure 7ab for Experiments 21 and 23, respectively. The experi-
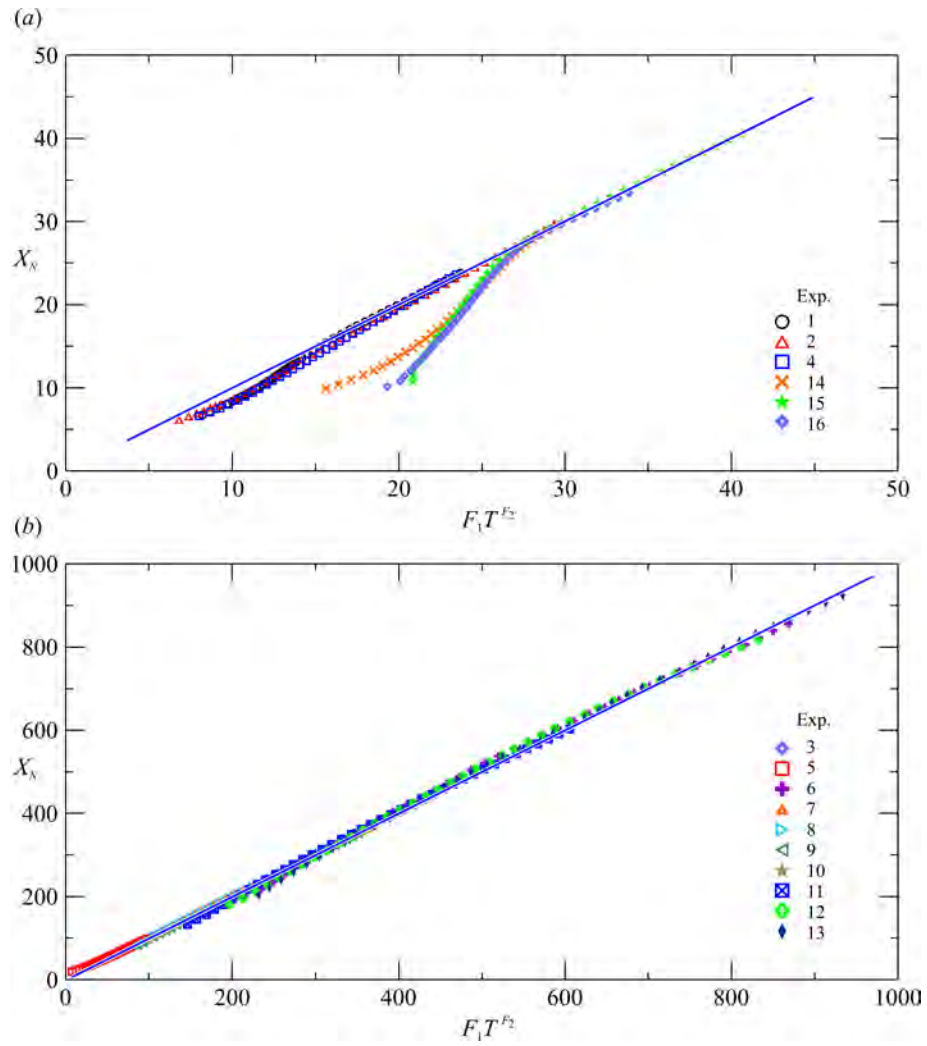
19

Figure 5: Experimental (symbols) versus theoretical (solid lines) front position for power-law fluids and (a) $\alpha = 0$, (b) $\alpha = 1$.

mental profile is smoother than the theoretical one due the dominant role of surface tension and free surface inclination with respect to the bottom inclination; it is also usually thicker, as a consequence of the three dimensional nature of the flow near the front. In this region, the inner solution of Huang and Garcia [3] could be adopted for a more realistic description of the profile; we neglect this local effect because we are interested in the overall dynamics of the current. Note that the peak of the thickness of the current at the front is completely smoothed out, presumably as an effect of the yield stress because power-law fluid currents in inclined channels still show the peak (see Longo et al. [16]). The streamwise surface velocity is shown in Figure 8 for Experiment 23. The streamwise velocity in the mid longitudinal cross section is characterised by several oscillations associated withthe free surface chevrons. Along transverse cross-sections, the velocity distribution is uniform in the core of the current and rapidly decays to zero near the contact line with the channel bottom. This is not consistent with eq. (30), which predicts a profile that reflects the bottom shape. However, it is necessary to consider that the transverse dynamics, which are completely neglected in the present model, smooth the velocity gradient by transferring momentum from the high velocity (in the mid-section of the channel) towards the low speed regions (the lateral walls).

The assumption $h/W << 1$ required by the theoretical model was not respected for all experiments nor for the entire duration of individual experiments. Remarkably, the solutions derived in the context of the approximation prove quite robust in interpreting results at the limit of the range of validity of the assumption and even beyond. This is quite common in the abundant literature on viscous gravity currents and porous gravity currents.

21

#	α	n	$\widetilde{\mu}$	τ_y	ρ	q	
			$(\mathrm{Pa\,s}^n)$	(Pa)	$(\mathrm{kg\,m}^{-3})$	$(\mathrm{ml\,s}^{-\alpha})$	
21	1	0.63 ± 0.03	0.88 ± 0.07	5.6 ± 0.4	1000	11.4	Carb (0.9%)
22	1	0.63	0.88	5.6	1000	24.9	Carb (0.9%)
23	1	0.42 ± 0.02	2.8 ± 0.2	18.4 ± 0.3	1020	39.7	Xanth (1%)
24	1	0.42	2.8	17.8 ± 0.5	1020	42.6	Xanth (1%)
26	1	0.20 ± 0.01	7.9 ± 0.4	6.4 ± 0.4	1018	9.6	Xanth (0.8%)
27	1	0.20	7.9	6.4	1018	18	Xanth (0.8%)
28	1	0.20	7.9	6.4	1018	42	Xanth (0.8%)
29	1	0.53 ± 0.02	1.7 ± 0.1	3.5 ± 0.4	1000	20.3	Carb (1.8%)
30	1	0.53	1.7	3.5	1000	32.7	Carb (1.8%)
31	1	0.53	1.7	3.5	1000	10.2	Carb (1.8%)

Table 2: Parameter values for the experiments with HB fluids. The last column indicates the fluid: water and Carbopol 980 (Carb), water and Xanthan (Xanth). The uncertainty listed for the rheometric parameters refers to one standard deviation.
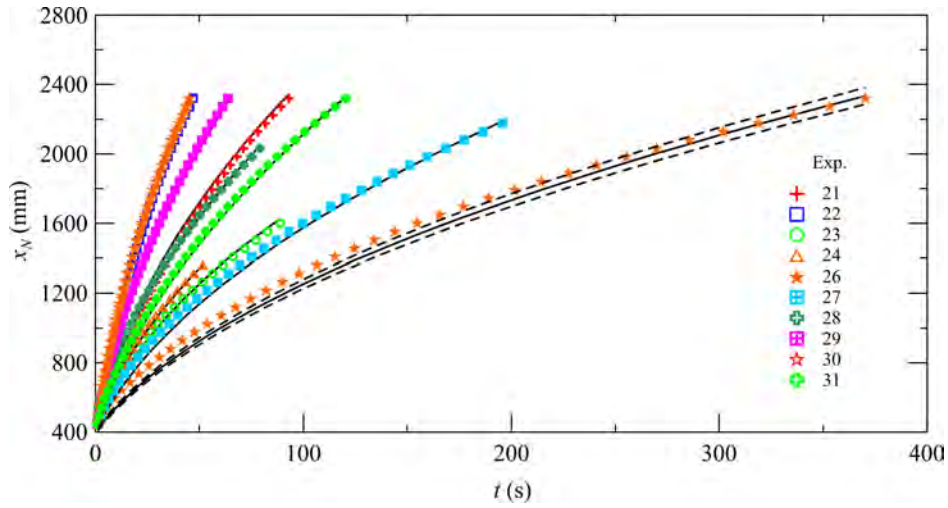

Figure 6: Experimental (symbols) versus theoretical (solid lines) front position for HB fluids and $\alpha = 1$. The dashed lines are the confidence limits of the theoretical model applied to one of the experiments.
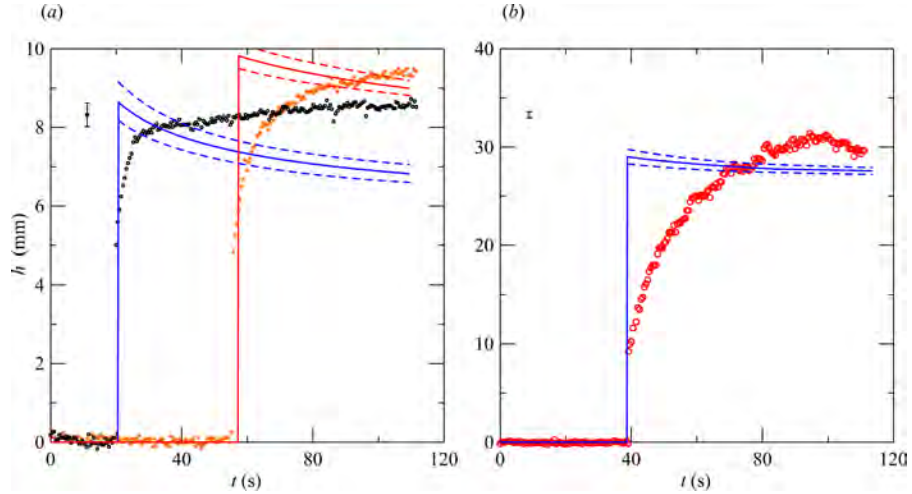
22

Figure 7: HB fluids. (a) The current thickness for Experiment 21 at 125 cm and 200 cm from the virtual origin, and (b) for Experiment 23 at 125 cm from the virtual origin. Experimental (symbols) versus theoretical (solid curves) values. The error bars indicate one standard deviation, the dashed curves are the confidence limits.
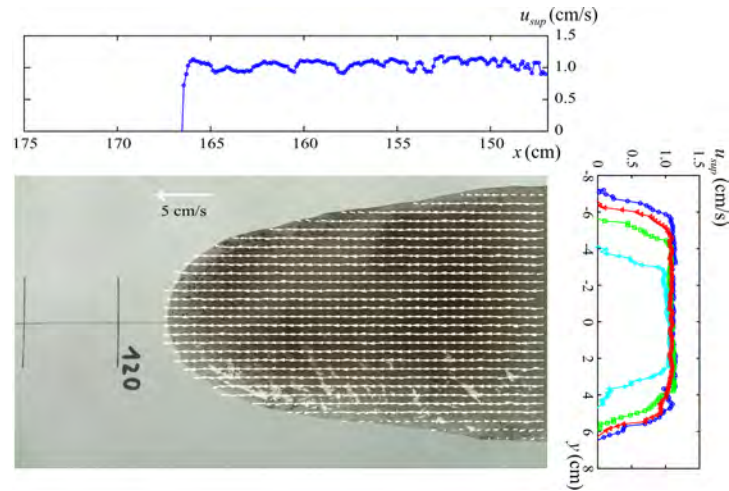

Figure 8: Surface streamwise velocity for Experiment 23. The upper panel depicts the velocity at $y = 0$, the right panel depicts the velocity at $x = 150$ (circles), 155 (triangles), 160 (squares), and 165 cm (diamonds). The values are averaged over a strip 0.8 cm wide.

23

5. Conclusions

We presented a theoretical model for the confined laminar flow of a gravity current of non-Newtonian fluid in a channel with a variable cross section and a variable bottom slope. The fluid is described by a Herschel-Bulkley model, including the power-law and Newtonian models as special cases. The problem is solved with the method of characteristics, either numerically (in the most general case of a nonzero yield stress) or analytically for power-law/Newtonian fluids.

The theory was tested against laboratory experiments; in general, experimental results for the rate of advancement of the current compare successfully with the theoretical formulation. The numerical approach reproduces the propagation of non-Newtonian currents at all times. The self-similar solution captures the behaviour of the front of power-law currents for constant flow rate, while it exhibits discrepancies at early times for instantaneous injection. The profile of the current is underestimated by the theory due to the three dimensional nature of the flow near the front, which induces a typical tongue shape in the horizontal projection.

The rheometry of the fluids proves to be essential in interpreting the flow behaviour and in comparing theory and experiments. In fact, the three parameters of the HB model show an interchangeable role in that different combinations of parameter values fit the experimental results equally well. Our tests highlight the crucial role of the yield stress, and suggest that it should be measured using a direct method. Indirect measurements of the yield stress on the base of rheometric data and without preventing slip are prone to error.

Our model captures the main features of natural phenomena such as debris, mud, and lava viscous flows down a slope. These environmental flows are usually channelised and often develop in self-formed channels due to erosion or deposits, with the latter forming levees. Typically, along the flow direction these channels exhibit a progressive reduction of the bottom slope and a widening cross section. These features are included in the model formulation and allow for a quick assessment of the spatiotemporal development of the gravity current, which can be used as a benchmark for more complex numerical models.

Possible extensions include (i) an analysis of the geometries of channels self-formed by viscous, non-Newtonian currents. This analysis seems interesting because it allows the prediction of the front speed and involves an

equilibrium model similar to that developed for rivers with mobile bottoms with further complexities due to the changing nature of the fluid rheology; (ii) the adoption of more realistic rheological equations, including a time dependence due to either the fluid nature or non-isothermal conditions; (iii) spatial variation of the fluid rheology associated with deposits of some components of the fluid or mixing of the initial current fluid with the eroded material; (iv) a model refinement close to the front; (v) an in-depth analysis of the free surface instabilities, which are expected to influence the shearing flow. These free surface instabilities also favour the fracturing of the plug flow layer, facilitating the exchange of chemicals and heat (e.g., lava flow) between the current and the overlying atmosphere. In particular, the inclusion of a spatial variation of the fluid rheology due to temperature variations is a challenging task because it requires an additional thermal balance equation and the estimation of additional parameters.

Appendix A. The rheometry of the fluids

The rheological behaviour of all fluids employed was assessed using a strain-controlled rheometer (coaxial cylinders Haake RT 10 RotoVisco). For Ostwald-de Waele shear-thinning and shear-thickening fluids, the flow behaviour index n and the consistency coefficient $\widetilde{\mu}$ were obtained by fitting a power-law to the measured data in the expected shear rate range.

For HB fluids, measurements are more complex and care is necessary to evaluate three model coefficients, in particular the yield stress. The reality of yield stress in fluids has been long debated, but this aspect seems of minor interest here, as an effective model of the fluid is necessary. As Carbopol was employed in our experiments, it is worth noting that for Carbopol 980 mixtures no yield stress was detected by Roberts and Barnes [40]. However, their measurements at high shear rate could be approximated by the HB model. Piau [41] conducted a detailed review on the variegate techniques used in measuring the properties of Carbopol gels, concluding that they can be adequately described by the HB model by ignoring elasticity, normal shear stresses and transients.

When dealing with HB fluids, the coaxial cylinders of the rheometer (cup and rotor according to DIN 53019, with internal radius equal to 19.36 mm and external radius equal to 21 mm) were roughened by sticking small strips (1 mm large, 0.1 mm thick) of Sellotape in the axial direction on both cylinders, to prevent slip. Although this method of increasing the roughness is uncon-
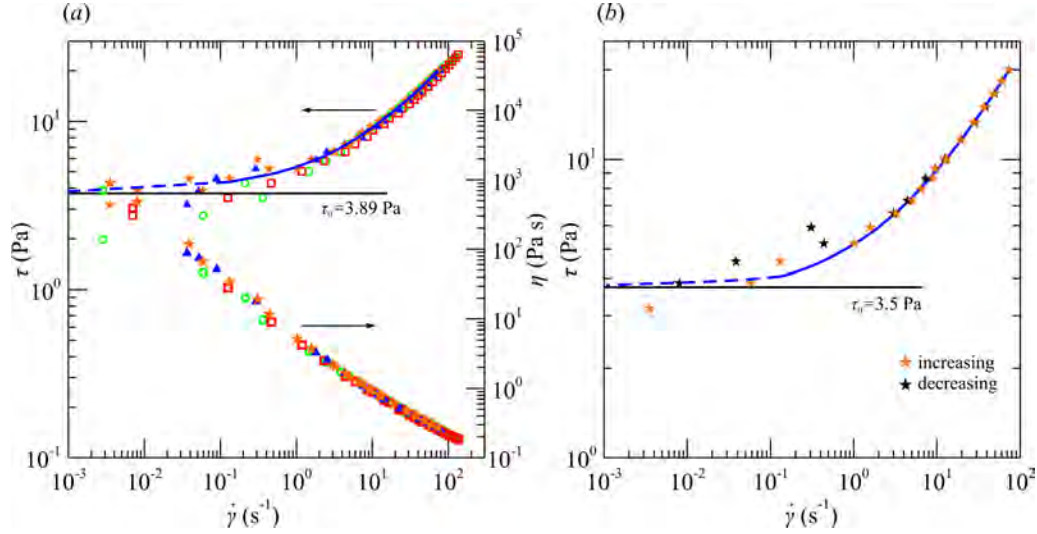
Figure A.9: (*a*) A plot of the shear stress and of the apparent viscosity versus shear rate for a Carbopol 980 mixture (1.8% non-neutralized). Several cycles were performed with the same sample, with increasing and decreasing torque. The solid line is the fitted HB model; (*b*) fitting to the HB model by measuring independently the yield stress with a direct method.

ventional, it is effective in preventing the slip as confirmed by comparing the rheometry data with and without Sellotape stripes, see [29]. The fitting of the function $\tau = \tau_0 + \widetilde{\mu}\dot{\gamma}^n$ to the experimental points, after correction of the apparent shear rate (see, e.g., [42]), gave the three parameters τ_0, $\widetilde{\mu}$ and n. Figure A.9*a* shows the shear stress and apparent viscosity versus shear rate for the mixture of Carbopol 980 (1.8% non-neutralized). The fitting with the HB model results in $\tau = 3.89 + 1.45\dot{\gamma}^{0.56}$, with the standard deviation of the parameters equal to $\sigma_{\tau_0} = 0.24\,\mathrm{Pa}$, $\sigma_{\widetilde{\mu}} = 0.13\,\mathrm{Pa\,s}^n$, and $\sigma_n = 0.02$. Figure A.9*b* shows the fitting to the HB model by evaluating a priori the yield stress with a direct method and then fitting the two remaining parameters.

In fact, the yield stress was also measured using two different direct methods, based on the static stability of a layer of fluid of known thickness on an inclined plane [43]. A layer of fluid was spread with a uniform thickness in a wide rectangular channel on a plane which could be slowly tilted by a DC motor (inclination rate less than $0.05°\mathrm{s}^{-1}$), with the instantaneous inclination measured by a $0.1°$ accurate electronic level. The free surface was seeded with small sand particles to facilitate the detection of the motion, and the bottom was covered with sand paper to prevent slip. Both particles and the

display of the level were recorded with the HD video camera, and the images were post processed with a Particle Image Velocimetry software to measure the free surface velocity in a restricted area located far from the walls. Figure A.10a shows a photograph of the apparatus, and Figure A.10bcd shows the free surface velocity measured along the maximum inclination for three different tests. The data are dispersed because no filtering or interpolation was applied to the extracted velocity vectors. The results for the six tests (four with a layer thickness equal to 5.7 mm and two with a layer thickness of 3.8 mm) are depicted in Figure A.11a, with error bars corresponding to ± 1 standard deviation (STD). The significant time increment of the measured yield stress can be attributed to the progressive evaporation of the water. In fact, the setup of each test (flattening the layer of fluid, mounting the electronic level, preparing the video camera) required up to 10 minutes. The difference in the results between experiments with different layer thicknesses can be attributed to the different importances of the experimental interferences and spurious effects.

A second method was based on measuring the residual thickness of fluid in the channel using an ultrasound distance metre after stopping the fluid injection. Waiting approximately 10 minutes, a complete stop of the fluid was observed. Then, measurements were taken in five different locations (except for one of the experiments, in which only three sections were measured). The results are shown in Figure A.11b for three experiments. The resulting values of yield stress are much more coherent than those obtained with the tilting plane, even though the residual thickness of the fluid layer in the central section of the channel is proportionally larger than in the other sections. As a consequence, there is an over prediction of the yield stress value. This phenomenon can be attributed to the fluid wave travelling from the inlet to the outlet of the channel after stopping the injection and to the transverse flow towards the centre of the cross section. In addition, the progressive evaporation of the water increases the yield stress and modifies the critical depth of the current. As a result, the final profile of the fluid at rest is controlled by (i) the process of progressive flow arrest, and (ii) the increment of the yield stress due to water evaporation. The two methods used for direct determination of the yield stress provided different results, but the second method gave a value in better agreement with the extrapolation of the rheometric measurements. The parameters of the HB model for the Carbopol 980 mixture (1.8% non-neutralised) were thus computed by imposing a yield stress $\tau_0 = 3.5\,\mathrm{Pa\,s}$, equal to the average value of the results of the thickness
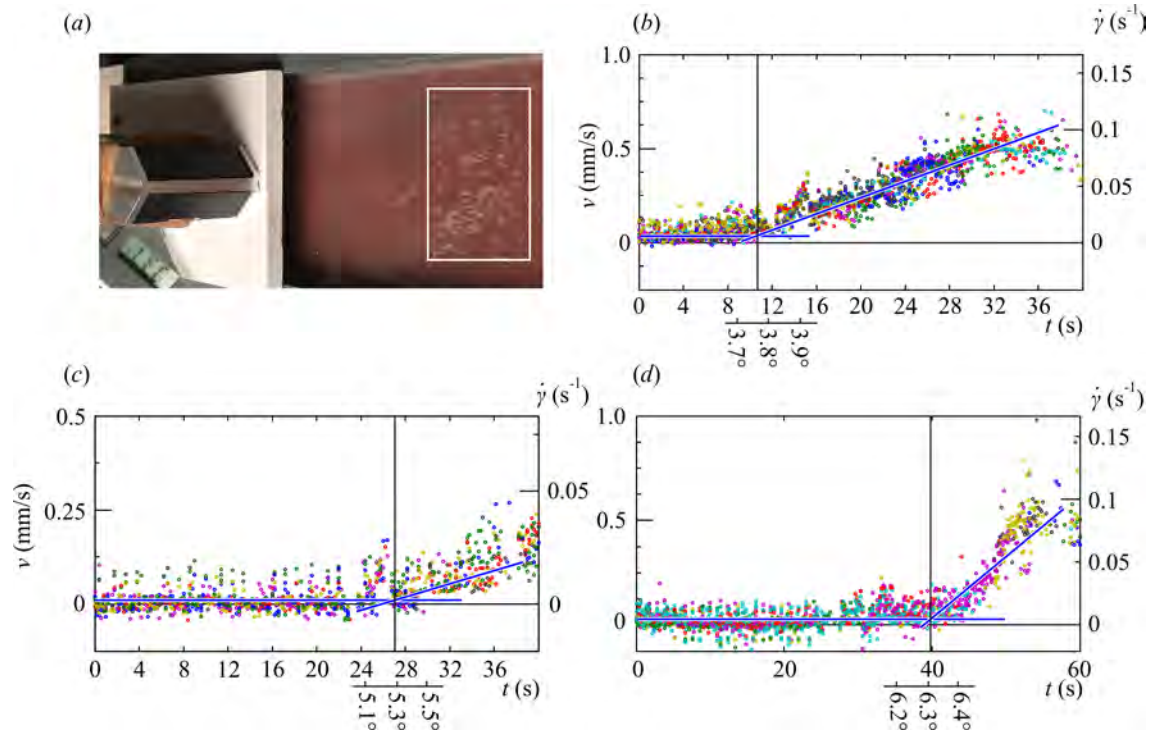
Figure A.10: (a) An image of the apparatus used for the direct measurement of the yield stress, with the display of the electronic level mirrored in the lower left corner. The rectangle indicates the area of PIV elaboration to extract the free surface velocity (the vectors indicate the instantaneous velocity of the free surface), with a spatial resolution equal to 6.5 pixels/mm. The plots of the free surface velocity versus time and plane inclination for a Carbopol 980 mixture (1.8% non-neutralized) are shown for (b) Experiment 2r, (c) Experiment 3r, and (d) Experiment 4r. The solid lines indicate the fitted free surface velocity, the vertical solid line indicates the assumed start of flow motion and the right vertical axis is the average shear rate obtained by dividing the free surface velocity and the starting thickness of the layer, neglecting its reduction in time. The thickness of the layer was set to 5.7 mm.
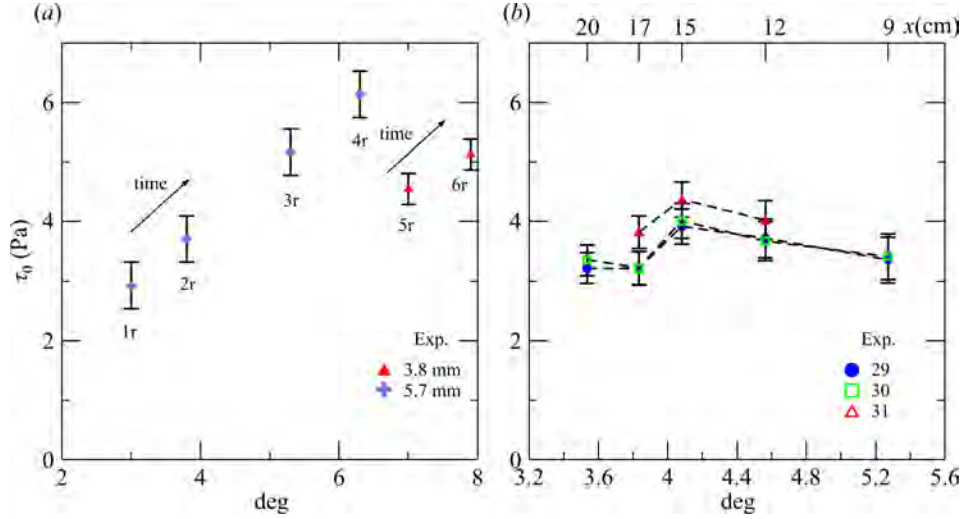
28

Figure A.11: Yield stress measured (a) using a tilting plane with a fixed initial thickness of fluid, and (b) on the basis of the residual thickness of the fluid in five sections of the channel 10 minutes after stopping the injection. The error bars correspond to ± 1 STD.

of the residual layer in the experimental channel, and fitting the curve to the rheometric experimental data, resulting in $\tau = 3.5 + 1.7\dot{\gamma}^{0.53}$ Pa. The same procedure was also used for the other yield stress fluids.

Upon observing the rheological behaviour of the fluids of interest over time, we noted that the rheology of Xhantan gum mixtures exhibits some time dependence, while Carbopol mixtures are essentially free of this phenomenon, as earlier noted by Piau [41]. Correspondingly, the former mixtures are expected to show a poorer agreement with the present model (based on time-independent rheological characterisation of the fluid) than the latter, a fact that was confirmed by our experiments.

The mass density was measured using a hydrometer or a pycnometer, with a relative uncertainty of 0.1%.

Appendix B. Discussion of the theoretical results: front velocity of power-law currents

The parameter space of the exponent F_2 modulating the current extension with time in eq. (23) is explored in Table B.3. First (row 1), it is observed that the expression of F_2 is valid below a limit value ω_e of the parameter ω describing the longitudinal slope variation. The limit value ω_e is strictly

29

positive, indicating that the solution is valid for any combination of channel shape (k), longitudinal variation (b) and fluid rheology (n), when the channel slope is decreasing ($\omega < 0$). The same is true for an increasing channel slope ($\omega > 0$) only when the limit value ω_e is not exceeded.

Second, Table B.3 (row 2) shows that the current is decelerated or accelerated ($F_2 \lessgtr 0$) depending on a critical value α_a of the volumetric rate of increase α. This is true for all negative slope variations ($\omega < 0$) and for positive slope variations not exceeding a limit value ω_a with $0 < \omega_a < \omega_e$. In the range $\omega_a < \omega < \omega_e$, the current is accelerated for any value of α, as the effect of the increasing channel slope prevails over the widening of the cross section. The critical value α_a depends also on the rheology (n), whereas it does not for a constant slope channel [16].

Third, the dependence of F_2 on the model parameters is investigated upon taking partial derivatives with respect to α, n, k, b, and ω (rows 3-7 of Table B.3). The propagation rate F_2 increases with α for all combinations of n, k, b and ω because the current volume is larger. The propagation rate F_2 is independent of the fluid rheology (n) when the volumetric increase α equals another critical value α_n, and the channel slope is in an intermediate range of the slope variation parameter, $\omega_{n1} - \omega_{n2}$, including both negative and positive values. In the same range of ω, F_2 increases/decreases with n for a slow ($\alpha < \alpha_n$) or fast ($\alpha > \alpha_n$) increase of current volume. Beyond the upper (positive) threshold ω_{n2}, F_2 decreases with n irrespective of α; the reverse is true below the lower (negative) threshold. This complex dependence of F_2 on n reflects the interplay of gravitational, viscous, and mass balance effects.

Similarly, the dependency of F_2 on the channel shape k is governed by a critical value α_k of the volumetric parameter α and two limit values of ω and b, ω_k and b_k. When these two threshold are not exceeded (decreasing or moderately increasing slopes and moderate widening), the propagation rate F_2 decreases/increases with k for a slow ($\alpha < \alpha_k$) or fast ($\alpha > \alpha_k$) volumetric increase. This dependency, which has already been observed for channels with constant slope ($\omega = 0$), reflects the relative importance of the competing effects of mass balance and viscous resistances. Beyond the upper (positive) threshold ω_k, F_2 decreases with k irrespective of α and b; beyond the upper threshold b_k, F_2 decreases with k irrespective of α.

Finally, the propagation rate increases with increasing ω for any α, k, n, and b and decreases with increasing b for any α, k, n, and ω. This is true because a greater slope parameter ω always produces faster currents, and a rapid widening of the cross section is associated with slower currents.

For $b = 0$, all critical values of α and limit parameters reduce to those predicted by Longo et al. [16].

$$
\begin{cases}
F_2 & \dfrac{\alpha k(n+1) + n(k+1)}{n(k+1) + k(n+1) + b(k-1)(n+1) - \omega(k+1)} \\[2ex]
F_2 > 0 & \omega < \omega_e \\[1.5ex]
\omega_e & n(k+1) + k(n+1) + b(k-1)(n+1)
\end{cases}
$$

$$
\begin{cases}
F_2 - 1 < 0 & \omega \le \omega_a \wedge \alpha < \alpha_a \\[1ex]
F_2 - 1 = 0 & \omega \le \omega_a \wedge \alpha = \alpha_a \\[1ex]
F_2 - 1 > 0 & (\omega_a < \omega < \omega_e \wedge \forall \alpha) \vee (\omega \le \omega_a \wedge \alpha > \alpha_a) \\[1ex]
\omega_a & k(n+1) + b(k-1)(n+1) \\[1.5ex]
\alpha_a & \dfrac{k(n+1) - \omega(k+1) + b(k-1)(n+1)}{k(n+1)}
\end{cases}
$$

$$
\dfrac{\partial F_2}{\partial \alpha} > 0 \qquad\qquad \forall n, k, b, \omega
$$

$$
\begin{cases}
\dfrac{\partial F_2}{\partial n} < 0 & (\omega_{n2} < \omega < \omega_e \wedge \forall \alpha) \vee (\omega_{n1} < \omega < \omega_{n2} \wedge \alpha > \alpha_n) \\[2ex]
\dfrac{\partial F_2}{\partial n} = 0 & \omega_{n1} < \omega < \omega_{n2} \wedge \alpha = \alpha_n \\[2ex]
\dfrac{\partial F_2}{\partial n} > 0 & (\omega \le \omega_{n1} \wedge \forall \alpha) \vee (\omega_{n1} < \omega < \omega_{n2} \wedge \alpha < \alpha_n) \\[2ex]
\omega_{n1} & -1 \\[2ex]
\omega_{n2} & \dfrac{k + b(k+1)}{k+1} \\[2ex]
\alpha_n & \dfrac{k + \beta(k-1) - \omega(k+1)}{k(\omega+1)}
\end{cases}
$$

(to be continued)

(continued)

$$
\begin{cases}
\dfrac{\partial F_2}{\partial k} < 0 & \begin{aligned}(\omega_k \leq \omega < \omega_e \wedge \forall \alpha) \vee (\omega < \omega_k \wedge b \geq b_k \wedge \forall \alpha) \vee \\ (\omega < \omega_k \wedge b < b_k \wedge \alpha < \alpha_k)\end{aligned} \\[2ex]
\dfrac{\partial F_2}{\partial k} = 0 & \omega < \omega_k \wedge b < b_k \wedge \alpha = \alpha_k \\[1.5ex]
\dfrac{\partial F_2}{\partial k} > 0 & \omega < \omega_k \wedge b < b_k \wedge \alpha > \alpha_k \\[1.5ex]
\omega_k & n \\[1.5ex]
b_k & \dfrac{n}{n+1} \\[2ex]
\alpha_k & \dfrac{n(1+2b)}{n - b(n+1) - \omega} \\[2ex]
\dfrac{\partial F_2}{\partial \omega} > 0 & \forall n, k, b, \alpha \\[2ex]
\dfrac{\partial F_2}{\partial b} < 0 & \forall n, k, \omega, \alpha
\end{cases}
$$

Table B.3: Dependence of the propagation rate F_2 on the model parameters for varying channel shapes and slopes. Row 1: conditions for $F_2 > 0$. Row 2: conditions for accelerated/constant speed/decelerated currents. Row 3: condition for F_2 increasing with α. Row 4: conditions for F_2 decreasing/constant/increasing with n. Row 5: conditions for F_2 decreasing/constant/increasing with k. Row 6: conditions for F_2 decreasing/constant/increasing with ω. Row 7: conditions for F_2 decreasing/constant/increasing with b. The shear rate on the right axis refers to the nominal thickness of the layer.

Appendix C. The slip condition

Slip at the wall is a characteristic of many fluids containing polymer chains, such as Xhantan gum based fluids (see, e.g., [44],[45]) and Carbopol. There are numerous semi-empirical models describing the slip effect [see, e.g., 46]; amongst these, we adopt the simple power-law Mooney's law [47]:

$$u_{slip} = s\tau_b^q, \tag{C.1}$$

where τ_b is the stress at the boundary and s and q are two empirical parameters. According to Piau [41], the exponent q should be close to one for smooth surfaces and less than one, between 0.57 and 0.37, for rough surfaces. The coefficient should be evaluated by experiments.

The presence of a slip increases the discharge with a further contribution given by

$$Q_{slip} = 2 \int_0^{W(x,t)} dy \int_{d(x,y,t)}^{h(x,t)} u_{slip}(x,y,t) dz \equiv$$

$$2s(\rho g \sin \beta_0)^q \left(\frac{x}{mx^*}\right)^{\omega q} \int_0^{W(x,t)} dy \int_{d(x,y,t)}^{h(x,t)} (h(x,t) - d(x,y,t))^q dz, \tag{C.2}$$

where the bounds of integration include the formerly defined 'no-flow' regions in Figure 2. The integral in eq. (C.2) admits a cumbersome analytic solution that can be expressed as

$$Q_{slip} = 2sh^{1+1/k+q} \left(\frac{x}{mx^*}\right)^{q\omega} (rx^b)^{1-1/k} (\rho g \sin \beta_0)^q f(k,q,b,r,x,h), \tag{C.3}$$

where $f(...)$ is a dimensionless function that can be expressed as a linear combination of dimensionless arguments. For $k = 2$ (the exponent describing the cross section used in our experiments, see §3) eq. (C.3) simplifies as

$$Q_{slip}|_{k=2} = sh^{3/2+q}(\pi r)^{1/2}x^{b/2} \left(\frac{x}{mx^*}\right)^{q\omega} (\rho g \sin \beta_0)^q \frac{\Gamma[2+q]}{\Gamma[5/2+q]} \tag{C.4}$$

Substituting eq. (32) and eq. (C.3) into eq. (11), and neglecting the

34

inclination of the free surface in the source term in eq. (5) results in

$$
h^{1/k} x^{b(1-1/k)} \frac{\partial h}{\partial t} + \frac{\partial}{\partial x} \left[\mathrm{B} \left[2 + \frac{1}{n}, 1 + \frac{1}{k} \right] \left(\frac{\rho g}{\widetilde{\mu}} \right)^{1/n} \frac{(\sin \beta_0)^{1/n}}{(m x^*)^{\omega/n}} \right.
$$
$$
\times x^{\omega/n + b(1-1/k)} h_s^{(1+1/k+1/n)} \left(h + \frac{n(k+1)}{k(n+1)} (h - h_s) \right)
$$
$$
\left. + s h^{1+1/k+q} \left(\frac{x}{m x^*} \right)^{q\omega} x^{b(1-1/k)} (\rho g \sin \beta_0)^q f \right] = 0, \quad \text{(C.5)}
$$

while the global continuity equation (15) and the boundary condition (13) are unvaried. The dimensionless form of eq. (C.5) is

$$
H^{1/k} X^{b(1-1/k)} \frac{\partial H}{\partial T}
$$
$$
+ \frac{\partial}{\partial X} \left[X^{\omega/n + b(1-1/k)} H_s^{1+1/k+1/n} \left(H + \frac{n(k+1)}{k(n+1)} (H - H_s) \right) \right.
$$
$$
\left. + c_s H^{1+1/k+q} X^{q\omega + b(1-1/k)} f \right] = 0, \quad \text{(C.6)}
$$

where $c_s = s t^* x^{*q-1} m^{-q\omega} (\rho g \sin \beta_0)^q$ is a non-dimensional coefficient relating the scales of the shear-plug flow and the scales of the slip flow. The global balance equation (19) is unchanged.

For $k = 2$, the function f depends only on the parameter q, with $f = \sqrt{\pi} \, \Gamma[2+q]/(2\Gamma[5/2+q])$ and eq. (C.6) becomes

$$
H^{1/2} X^{b/2} \frac{\partial H}{\partial T}
$$
$$
+ \frac{\partial}{\partial X} \left[X^{\omega/n + b/2} H_s^{3/2+1/n} \left(H + \frac{3n}{2n+2} (H - H_s) \right) + c_s' H^{3/2+q} X^{q\omega + b/2} \right] = 0,
$$
$$
\text{(C.7)}
$$

with $c_s' \equiv c_s \left. f \right|_{k=2} = s t^* x^{*q-1} m^{-q\omega} (\rho g \sin \beta_0)^q \sqrt{\pi} \, \Gamma[2+q]/(2\Gamma[5/2+q])$.

References

[1] J. E. Simpson, Gravity currents in the environment and the laboratory, Cambridge University Press, 1997.

[2] M. Chowdhury, F. Testik, Laboratory testing of mathematical models for high-concentration fluid mud turbidity currents, Ocean Eng. 38 (2011) 256–270.

[3] X. Huang, M. Garcia, A Herschel-Bulkley model for mud flow down a slope, J. Fluid Mech. 374 (1998) 305–333. doi:10.1017/S0022112098002845.

[4] N. Yilmaz, F. Testik, M. Chowdury, Laminar bottom gravity currents: friction factor-Reynolds number relationship, J. Hydraul. Res. 52 (2014) 545–558.

[5] J. Burger, R. Haldenwang, N. Alderman, Laminar and turbulent flow of non-Newtonian fluids in open channels for different cross-sectional shapes, J. Hydr. Eng. 85 (2015) 04014084–1–04014084–12.

[6] S. Saha, D. Salin, L. Talon, Low Reynolds number suspension gravity currents, Eur. Phys. J. E 36 (2013) 85–102.

[7] A. Scotto di Santolo, A. Pellegrino, A. Evangelista, Experimental study on the rheological behaviour of debris flow, Nat. Hazards Earth Syst. Sci. 10 (2010) 2507–2514.

[8] M. Filippucci, A. Tallarico, M. Dragoni, Role of heat advection in a channeled lava flow with power law, temperature-dependent rheology, J. Geophys. Res. 118 (2013) 2764–2776. doi:10.1029/2009JB006335.

[9] M. Ungarish, An Introduction to Gravity Currents and Intrusions, CRC Press, 2009.

[10] M. Chowdhury, F. Testik, Axisymmetric underflows from impinging buoyant jets of dense cohesive particle-laden fluids, J Hydraul. Eng. 141 (2015) 04014079–1–04014079–15.

[11] H. E. Huppert, The propagation of two-dimensional and axisymmetric viscous gravity currents over a rigid horizontal surface, J. Fluid Mech. 121 (1982) 43–58.

[12] H. E. Huppert, Flow and instability of a viscous current down a slope, Nature 300 (1982) 427–429.

[13] D. Takagi, H. E. Huppert, The effect of confining boundaries on viscous gravity currents, J. Fluid Mech. 577 (2007) 495–505.

[14] D. Takagi, H. E. Huppert, Viscous gravity currents inside confining channels and fractures, Phys. Fluids 20 (2008) 023104.

[15] S. Longo, V. Di Federico, L. Chiapponi, Non-newtonian power-law gravity currents propagating in confining boundaries, Environmental Fluid Mechanics 15 (3) (2015) 515–535. doi:10.1007/s10652-014-9369-9.

[16] S. Longo, V. Di Federico, L. Chiapponi, Propagation of viscous gravity currents inside confining boundaries: the effects of fluid rheology and channel geometry, Proceedings of the Royal Society of London A: Mathematical, Physical and Engineering Sciences 471 (2178). doi:10.1098/rspa.2015.0070.

[17] P. Coussot, Yield stress fluid flows: A review of experimental data, Journal of Non-Newtonian Fluid Mechanics 211 (2014) 31–49.

[18] A. Hogg, G. Matson, Slumps of viscoplastic fluids on slopes, Journal of Non-Newtonian Fluid Mechanics 158 (2009) 101–112.

[19] D. Vola, F. Babik, J.-C. Latch, On a numerical strategy to compute gravity currents of non-Newtonian fluids, J. Comp. Phys. 201 (2004) 397–420.

[20] N. Balmforth., R. Craster, A. Rust, R. Sassi, Viscoplastic flow over an inclined surface, Journal of Non-Newtonian Fluid Mechanics 139 (2006) 103–127.

[21] C. C. Mei, M. Yuhi, Slow flow of a Bingham fluid in a shallow channel of finite width, J. Fluid Mech. 431 (2001) 135–159. doi:10.1017/S0022112000003013.

[22] A. Cantelli, Uniform flow of modified Bingham fluids in narrow cross sections, J Hydraul. Eng. 135 (2009) 640–650.

[23] C. Ancey, S. Cochard, The dam-break problem for Herschel-Bulkley viscoplastic fluids down steep flumes, Journal of Non-Newtonian Fluid Mechanics 158 (2009) 18–35.

[24] G. Chambon, A. Ghemmour, M. Naiim, Experimental investigation of viscoplastic free-surface flows in a steady uniform regime, J. Fluid Mech. 754 (2014) 332–364.

[25] I. Ionescu, Viscoplastic shallow flow equations with topography, Journal of Non-Newtonian Fluid Mechanics 193 (2013) 116–128.

[26] D. Montgomery, W. Dietrich, Channel initation and the problem of lanscape scale, Science 255(5046) (1992) 826–830.

[27] J. Robertson, R. Kerr, Solidification dynamics in channeled viscoplastic lava flows, J. Geophys. Res. 117 (2012) B07206. doi:10.1029/2009JB006335.

[28] F. Mazzarini, M. Pareschi, M. Favalli, I. Isola, S. Tarquini, E. Boschi, Morphology of basaltic lava channels during the mt. etna september 2004 eruption from airborne laser altimeter data, Geophys. Res. Lett. 32 (2005) L04305.

[29] H. Barnes, A review of the slip (wall depletion) of polymer solutions, emulsions and particle slip in viscometers -its cause, character, and cure, Journal of Non-Newtonian Fluid Mechanics 56 (1995) 221–251.

[30] A. L. Harris, J. Dehn, S. Calvari, Lava effusion rate definition and measurement: a review, Bull. Volcanol. 70 (2007) 1–22.

[31] W. Wood, Introduction to numerical methods for water resources, Oxford University Press, 1993.

[32] K. F. Liu, C. C. Mei, Slow spreading of a sheet of Bingham fluid on an inclined plane, J. Fluid Mech. 207 (1989) 505–529. doi:10.1017/S0022112089002685.

[33] S. Cintoli, R. Ugarelli, V. Di Federico, Laminar flow of a Herschel-Bulkley fluid in channels of finite width, in: Proceedings 32nd IAHR World Congress "Harmonizing the Demands of Art and Nature in Hydraulics", 1-6 July 2007, Venice, Italy, 2007, pp. 1–10.

[34] K. Hutter, Theoretical Glaciology, D. Reidel Publishing Company, 1983.

[35] I. C. Walton, S. H. Bittleston, The axial flow of a Bingham plastic in a narrow eccentric annulus, Journal of Fluid Mechanics 222 (1991) 39–60. doi:10.1017/S002211209100099X.

[36] N. Balmforth, R. Craster, A consistent thin-layer theory for Bingham plastics, Journal of Non-Newtonian Fluid Mechanics 84 (1) (1999) 65 – 81. doi:http://dx.doi.org/10.1016/S0377-0257(98)00133-5.

[37] S. Longo, Experiments on turbulence beneath a free surface in a stationary field generated by a Crump weir: free-surface characteristics and the relevant scales, Experiments in Fluids 49 (6) (2010) 1325–1338. doi:10.1007/s00348-010-0881-5.

[38] S. Longo, Experiments on turbulence beneath a free surface in a stationary field generated by a Crump weir: turbulence structure and correlation with the free surface, Experiments in Fluids 50 (1) (2011) 201–215. doi:10.1007/s00348-010-0921-1.

[39] A. Slim, N. Balmforth, R. Craster, J. Miller, Surface wrinkling of a channelized flow, Proceedings of the Royal Society of London A: Mathematical, Physical and Engineering Sciences 465 (2101) (2009) 123–142. doi:10.1098/rspa.2008.0142.

[40] G. Roberts, H. Barnes, New measurements of the flow curves for carbopol dispersions without slip artifacts, Rheol. Acta 40 (2001) 499–503.

[41] J. Piau, Carbopol gels: Elastoviscoplastic and slippery glasses made of individual swollen sponges Meso- and macroscopic properties, constitutive equations and scaling laws, Journal of Non-Newtonian Fluid Mechanics 144 (1) (2007) 1 – 29. doi:http://dx.doi.org/10.1016/j.jnnfm.2007.02.011.

[42] Q. D. Nguyen, D. Boger, Measuring the flow properties of yield stress fluids, Annual Review of Fluid Mechanics 24 (1992) 47–88.

[43] P. Uhlherr, K. Park, C. Tiu, J. Andrews, Yield stress from fluid behaviour on an inclined plane, in: Adv. in Rheology, MexicoCity 1984, Vol. 2, 1984, pp. 183–190.

[44] L. De Vargas, O. Manero, On the slip phenomenon of polymeric solutions through capillaries, Polymer Engineering & Science 29 (18) (1989) 1232–1236. doi:10.1002/pen.760291804.

[45] L. Valdez, M. A.and Yeomans, F. Montes, H. Acuña, A. Ayala, Influence of temperature on the slip velocity of semidilute xanthan gum solutions, Rheologica Acta 34 (5) (1995) 474–482. doi:10.1007/BF00396560.

[46] N. Balmforth, A. Burbidge, R. Craster, J. Salzig, A. Shen, Visco-plastic models of isothermal lava domes, J. Fluid Mech. 403 (2000) 37–65.

[47] M. Mooney, Explicit formulas for slip and fluidity, J. Rheol 2 (1931) 210–222.